



The Roles of Fluid Compression and Shear in Electron Energization during Magnetic Reconnection

Xiaocan Li¹ , Fan Guo^{1,2} , Hui Li¹ , and Joachim Birn^{3,4} ¹ Los Alamos National Laboratory, Los Alamos, NM 87544, USA; xiaocanli@lanl.gov² New Mexico Consortium, 4200 West Jemez Road, Los Alamos, NM 87544, USA³ Space Science Institute, Boulder, CO 80301, USA⁴ Guest Scientist, Los Alamos National Laboratory, Los Alamos, NM 87544, USA

Received 2018 January 7; revised 2018 January 30; accepted 2018 January 31; published 2018 March 9

Abstract

Particle acceleration in space and astrophysical reconnection sites is an important unsolved problem in studies of magnetic reconnection. Earlier kinetic simulations have identified several acceleration mechanisms that are associated with particle drift motions. Here, we show that, for sufficiently large systems, the energization processes due to particle drift motions can be described as fluid compression and shear, and that the shear energization is proportional to the pressure anisotropy of energetic particles. By analyzing results from fully kinetic simulations, we show that the compression energization dominates the acceleration of high-energy particles in reconnection with a weak guide field, and the compression and shear effects are comparable when the guide field is 50% of the reconnecting component. Spatial distributions of those energization effects reveal that reconnection exhausts, contracting islands, and island-merging regions are the three most important regions for compression and shear acceleration. This study connects particle energization by particle guiding-center drift motions with that due to background fluid motions, as in the energetic particle transport theory. It provides foundations for building particle transport models for large-scale reconnection acceleration such as those in solar flares.

Key words: acceleration of particles – accretion, accretion disks – magnetic reconnection – Sun: corona – Sun: flares

1. Introduction

Magnetic reconnection is a major mechanism that drives the release of magnetic energy in space and astrophysical plasmas (Zweibel & Yamada 2009). For example, magnetic reconnection converts 10%–50% of the magnetic energy into plasma kinetic energy within 10^{2-3} s (Lin & Hudson 1976) and heats solar coronal plasma from ~ 1 MK to up to over 30 MK during solar flares (Caspi & Lin 2010; Longcope et al. 2010). Besides heating, observations indicate that magnetic reconnection can accelerate about 10% of electrons (Oka et al. 2013, 2015) or even the entire electron population in a solar flare region (more than 10^{36} electrons) into a nonthermal distribution (Krucker et al. 2010; Krucker & Battaglia 2014). Such efficient particle acceleration over a large-scale reconnection region is an important unsolved problem in the study of reconnection.

Previous reconnection studies have identified that particles are accelerated close to the reconnection X -point (Hoshino et al. 2001; Drake et al. 2005; Fu et al. 2006; Oka et al. 2010; Egedal et al. 2012, 2015; Wang et al. 2016), in contracting magnetic islands (Drake et al. 2006; Oka et al. 2010), and also in island-merging regions (Oka et al. 2010; Liu et al. 2011; Drake et al. 2013; Nalewajko et al. 2015). At the X -points, particles get accelerated by streaming along the nonideal electric field. In the contracting and merging magnetic islands, the acceleration closely resembles *Fermi*-type processes. In order to clarify the acceleration mechanism, some recent works calculated the energy gain by summing over particle motions under the guiding-center approximation and identified

curvature drift as the primary particle acceleration mechanism during reconnection (Dahlin et al. 2014; Guo et al. 2014, 2015; Li et al. 2015; Zhou et al. 2015; Beresnyak & Li 2016). This drift acceleration is similar to the *Fermi* process because particles gain energy proportional to their kinetic energy when they are bouncing between two sides of a magnetic island and in island-merging regions.

To understand particle acceleration in a large-scale reconnection layer, an important task is to develop a statistical transport theory that includes the primary acceleration mechanisms. In shock acceleration theory, the Parker transport equation has provided the basic description for the acceleration and transport of energetic particles in the shock region, where adiabatic compression is the leading acceleration mechanism (Parker 1965; Blandford & Eichler 1987). Acceleration due to velocity shear and fluid inertia have been considered as higher-order effects (e.g., Earl et al. 1988; Zank 2014). Several reconnection studies have attempted to develop similar kinetic equations to evolve electron distribution. The most common approach is to derive a reduced kinetic equation from the guiding-center drift kinetic equation by assuming double-adiabatic invariants: the magnetic moment and the parallel action integral (Drake et al. 2006, 2013; Egedal et al. 2013; Montag et al. 2017). This approach keeps the essential acceleration mechanism—field line shortening due to island contraction and coalescence—and can describe the evolution of trapped and passing electrons close to the reconnection X -line (Drake et al. 2013; Montag et al. 2017) and explained the generation of pressure anisotropy close to the reconnection X -line well (Egedal et al. 2013). If one neglects the heat fluxes, the CGL closure based on the double-adiabatic assumption predicts that the plasma heating can be expressed in terms of plasma density and magnetic field strength (Chew et al. 1956).



Original content from this work may be used under the terms of the [Creative Commons Attribution 3.0 licence](https://creativecommons.org/licenses/by/3.0/). Any further distribution of this work must maintain attribution to the author(s) and the title of the work, journal citation and DOI.

Montag et al. (2017) further showed that the plasma energization is due to the $d \ln B/dt$ and $d \ln n/dt$, where B is the magnetic strength and n is the plasma density. They included a finite compressibility in the reduced kinetic equation and found that the finite compressibility helps *Fermi* acceleration, producing a harder power-law spectrum.

Recently, by assuming the same adiabatic invariants, Zank et al. (2014) derived a comprehensive focused transport equation that incorporates an elaborate model with reconnection electric field, island contraction, and island coalescence for arbitrary particle scattering levels, and a Parker-type transport equation for the strong scattering limit, starting from a transformed Vlasov equation (Skilling 1975). This equation has then been used to explain the power-law distribution of energetic particles observed in the solar wind (Zank et al. 2014) and also the anomalous cosmic-ray (ACR) energy spectrum mediated by the reconnection processes downstream of the heliospheric termination shock (Zank et al. 2015). This approach does not assume incompressible plasma and clearly distinguishes the three acceleration mechanisms due to the mean field and plasma flow, but its connection with particle drifts is unclear. le Roux et al. (2015) derived a more general focused transport equation, including both mean and variance of the reconnection fields and plasma flow and starting from the standard guiding-center kinetic equation (Kulsrud 1983; le Roux & Webb 2009; Webb et al. 2009), and the theory now includes both incompressible and compressible energization. This approach clearly shows the connection between the energization due to particle drift motions (also reconnection electric field and betatron acceleration) and energetic particle acceleration due to the background plasma flow. However, the relative importance between the compression acceleration and other acceleration mechanisms is undetermined.

Recent resistive MHD simulations suggest that the compression effect is important for reconnection, especially when the plasma β or guide field (magnetic field component perpendicular to the reconnecting component) is low (Birn et al. 2012; Provornikova et al. 2016). Drury (2012) treated the acceleration of particles in reconnection similar to the diffusive shock acceleration and showed that compression is important for driving particle acceleration. Zank et al. (2014), le Roux et al. (2015), and Montag et al. (2017) have pointed out that the compression effect may be important for particle energization in reconnection regions. These appear to be in contradiction with some previous theories that assume the reconnection layer is incompressible (e.g., Drake et al. 2006, 2013; see also the discussion in de Gouveia Dal Pino & Kowal 2015).

A goal of this study is to clarify the importance of compressibility in particle energization in the magnetic reconnection layer using fully kinetic simulations that self-consistently evolve both low-energy “background” plasma and high-energy particles.

In this paper, we use moments of the Vlasov equation to derive the energization based on the fluid motions such as fluid compression and pressure-anisotropy-related shear effect. This approach becomes quite useful and meaningful when the system size is large enough (i.e., much larger than the typical kinetic scales). Using particle-in-cell (PIC) kinetic simulations, we evaluate the relative importance of different effects and quantify the influence of the guide field and plasma β in these processes. We find that compressional energization dominates the acceleration of high-energy particles when the guide field is

weak, and the compression and shear effects become comparable when the guide field is moderate (50% of the reconnecting component). Changing plasma β does not significantly alter the relative contribution of these energization terms. In Section 2, we show how the compression energization and shear energization terms emerge from previous analyses based on the currents induced by guiding-center drifts. The fully kinetic simulations and parameters are described in Section 3. In Section 4, we present simulation results and analyses for electron energization. In Section 5, we discuss the conclusions and the implications based on our simulation results.

2. Compressional Energization and Shear Energization

Instead of starting from the drift kinetic equation for energetic particles, we start from the Vlasov equation for the whole particle population in the inertial frame:

$$\partial_t f_s + \frac{\mathbf{p}}{m_s \gamma} \cdot \nabla f_s + q_s \left(\mathbf{E} + \frac{\mathbf{p}}{m_s \gamma} \times \mathbf{B} \right) \cdot \nabla_p f_s = 0, \quad (1)$$

where f_s is the phase space density, q_s is the particle charge, m_s is the particle rest mass for each species (proton or electron), \mathbf{p} is the particle momentum, $\gamma = \sqrt{1 + p^2/(m_s^2 c^2)}$ is the Lorentz factor, and \mathbf{E} and \mathbf{B} are electric and magnetic fields. To study the energization of the whole particle population, we first take the moments of this equation and obtain the conservation laws of charge, momentum, and energy, which are

$$\partial_t \rho_s + \nabla \cdot \mathbf{j}_s = 0, \quad (2)$$

$$\partial_t \mathbf{p}_s + \nabla \cdot \mathbf{T}_s = \rho_s \mathbf{E} + \mathbf{j}_s \times \mathbf{B}, \quad (3)$$

$$\partial_t \mathcal{E}_s + \nabla \cdot (c^2 \mathbf{p}_s) = \mathbf{j}_s \cdot \mathbf{E}, \quad (4)$$

where $\rho_s = \langle q_s \rangle_s$ is the charge density, $\mathbf{j}_s = \langle q_s \mathbf{p} / m_s \gamma \rangle_s$ is the current density, $\mathbf{p}_s = \langle \mathbf{p} \rangle_s$ is the momentum density, $\mathbf{T}_s = \langle \mathbf{p} \mathbf{p} / m_s \gamma \rangle_s$ is the stress tensor, $\mathcal{E}_s = \langle m_s c^2 \gamma \rangle_s$ is the particle energy density, and $\langle A \rangle_s \equiv \int d^3 p A f_s$ for a general physical quantity A . By assuming that the heat flux can be neglected, we truncate the fluid equation at the second-order moments. This is consistent with the renowned CGL closure (Chew et al. 1956). Equation (4) shows that particles gain energy through $\mathbf{j}_s \cdot \mathbf{E}$. Using the momentum conservation equation to evaluate the perpendicular component of the current density $\mathbf{j}_{s\perp}$ w.r.t to the local magnetic field, we found

$$\mathbf{j}_{s\perp} = -\frac{(\nabla \cdot \mathbf{P}_s) \times \mathbf{B}}{B^2} + \rho_s \frac{\mathbf{E} \times \mathbf{B}}{B^2} - n_s m_s \frac{d\mathbf{u}_s}{dt} \times \frac{\mathbf{B}}{B^2}, \quad (5)$$

where we used $n_s = \rho_s / q_s$, $\mathbf{u}_s = \mathbf{p}_s / (n_s m_s)$, $d/dt = \partial_t + \mathbf{v}_s \cdot \nabla$, and $\mathbf{T}_s = \mathbf{P}_s + \mathbf{v}_s \mathbf{p}_s$ with the pressure tensor \mathbf{P}_s and the species flow velocity $\mathbf{v}_s = \mathbf{j}_s / \rho_s$. The first term on the right is due to plasma drift caused by the pressure gradient force, the second term is due to $\mathbf{E} \times \mathbf{B}$ drift, and the last term is due to particle inertia. We assume that particles are well magnetized for simplicity, which leads to

$$\mathbf{P}_s = p_{s\perp} \mathbf{I} + (p_{s\parallel} - p_{s\perp}) \hat{\mathbf{b}} \hat{\mathbf{b}}, \quad (6)$$

where $p_{s\parallel} = \langle (\mathbf{v}_{\parallel} - \mathbf{v}_{s\parallel}) \cdot (\mathbf{p}_{\parallel} - \mathbf{p}_{s\parallel} / n_s) \rangle$ and $p_{s\perp} = 0.5 \langle (\mathbf{v}_{\perp} - \mathbf{v}_{s\perp}) \cdot (\mathbf{p}_{\perp} - \mathbf{p}_{s\perp} / n_s) \rangle$ are parallel and perpendicular pressures

w.r.t the local magnetic field, $\hat{\mathbf{b}} = \mathbf{B}/B$ is the unit vector along the local magnetic field, and \mathbf{l} is the unit dyadic. This description is not completely accurate in regions with weak magnetic fields and in the diffusion region because particles are not well magnetized. However, for sufficiently large systems, the effect of the asymmetric pressure tensor has a minor role in the energization during reconnection (Li et al. 2017). Then, the pressure gradient effect can be broken into

$$\begin{aligned} \mathbf{j}_{s\perp} = & -\frac{\nabla p_{s\perp} \times \mathbf{B}}{B^2} + (p_{s\parallel} - p_{s\perp}) \frac{\mathbf{B} \times (\mathbf{B} \cdot \nabla) \mathbf{B}}{B^4} \\ & + \rho_s \frac{\mathbf{E} \times \mathbf{B}}{B^2} - n_s m_s \frac{d\mathbf{u}_s}{dt} \times \frac{\mathbf{B}}{B^2}, \end{aligned} \quad (7)$$

where the first term is due to diamagnetic drift, and the second term is due to magnetic field curvature and is proportional to the pressure anisotropy. Equation (7) can be reorganized as

$$\begin{aligned} \mathbf{j}_{s\perp} = & p_{s\parallel} \frac{\mathbf{B} \times (\mathbf{B} \cdot \nabla) \mathbf{B}}{B^4} + p_{s\perp} \frac{\mathbf{B} \times \nabla B}{B^3} - \left[\nabla \times \frac{p_{s\perp} \mathbf{B}}{B^2} \right]_{\perp} \\ & + \rho_s \frac{\mathbf{E} \times \mathbf{B}}{B^2} - n_s m_s \frac{d\mathbf{u}_s}{dt} \times \frac{\mathbf{B}}{B^2}, \end{aligned} \quad (8)$$

where the first three terms are due to curvature drift, gradient drift, and perpendicular magnetization. Note that this expression is for the whole particle population and a similar expression could be obtained for energetic particles from the guiding-center drift kinetic equation (Kulsrud 1983; le Roux et al. 2015).

To evaluate the energy gain $\mathbf{j}_{s\perp} \cdot \mathbf{E}_{\perp}$, we use $\mathbf{j}_{s\perp}$ from Equation (7) and $\mathbf{E}_{\perp} = -\mathbf{v}_E \times \mathbf{B}$, where $\mathbf{v}_E = \mathbf{E} \times \mathbf{B}/B^2$ is the $\mathbf{E} \times \mathbf{B}$ drift. After some algebra, we found that

$$\begin{aligned} \mathbf{j}_{s\perp} \cdot \mathbf{E}_{\perp} = & \nabla \cdot (p_{s\perp} \mathbf{v}_E) - p_s \nabla \cdot \mathbf{v}_E \\ & - (p_{s\parallel} - p_{s\perp}) b_i b_j \sigma_{ij} + n_s m_s \frac{d\mathbf{u}_s}{dt} \cdot \mathbf{v}_E, \end{aligned} \quad (9)$$

where $p_s = (p_{s\parallel} + 2p_{s\perp})/3$ is the effective scalar pressure, $\sigma_{ij} = 0.5(\partial_i v_{Ej} + \partial_j v_{Ei} - (2\nabla \cdot \mathbf{v}_E \delta_{ij})/3)$ is the shear tensor for \mathbf{v}_E . The first term on the right is the flux term that does not contribute to the energization. We define the second term as the compressional energization, the third term as the shear energization, and the last term as the inertial energization. Note that le Roux et al. (2015) have shown similar energization terms (Equation (13) in their paper) by using the guiding-center drift kinetic equation, but they did not specifically point out the role of pressure anisotropy and fluid shear. Since current analysis employs the same two assumptions as the CGL closure, i.e., neglecting heat fluxes and assuming magnetized particles, the plasma energization shown in Equation (9) is consistent with other theories based on these assumptions (Montag et al. 2017; see the Appendix). We argue that \mathbf{v}_E is a proper choice of perpendicular plasma flow for studying particle energization by fluid motions. For a macroscopic system, \mathbf{v}_E is the leading-order drift motion among all drift motions in the plasma perpendicular flow (Hazeltine & Meiss 2003). It has been identified as the dominant perpendicular plasma flow velocity when deriving the transport equation for studying particle acceleration (le Roux et al. 2015). Even

for a relatively small-scale system as our kinetic simulations described in the next section, \mathbf{v}_E provides a common flow frame for both electrons and ions.

Our goal is twofold: (1) we want to test whether Equation (9) can describe the energization processes occurring in our PIC simulations of reconnection, and (2) we want to assess the relative importance of these three processes in electron energization. One can calculate the overall contributions to the plasma energization by compression, shear, and inertia to evaluate the relative importance of these terms. Furthermore, to study their energy dependence, for each particle in the simulations, one can calculate $\mathbf{v}_{\parallel} \cdot \mathbf{E}_{\parallel}$, $\mathbf{v}_{\perp} \cdot \mathbf{E}_{\perp}$, $-p \nabla \cdot \mathbf{v}_E$, $-(p_{\parallel} - p_{\perp}) b_i b_j \sigma_{ij}$, and $m_s (d\mathbf{u}_s/dt) \cdot \mathbf{v}_E$, where $p_{\parallel} = (\mathbf{v}_{\parallel} - \mathbf{v}_{s\parallel}) \cdot (\mathbf{p}_{\parallel} - \mathbf{p}_{s\parallel})$, $p_{\perp} = 0.5(\mathbf{v}_{\perp} - \mathbf{v}_{s\perp}) \cdot (\mathbf{p}_{\perp} - \mathbf{p}_{s\perp})$, and $p = (p_{\parallel} + 2p_{\perp})/3$ are the contributions of each particle to the parallel pressure, perpendicular pressure, and scalar pressure, respectively. One may then accumulate the single-particle quantities in a series of energy bins to examine the energy dependence of different energization effects. For high-energy particles, this approach is consistent with that used by the guiding-center drift kinetic equation (le Roux et al. 2015), which does not calculate each energetic particle's contribution to the pressure but the $\mathbf{v}_{\parallel} \cdot \mathbf{p}_{\parallel}$ and $\mathbf{v}_{\perp} \cdot \mathbf{p}_{\perp}/2$ terms. The energization terms shown in Equation (9) are consistent with the double-adiabatic theories.

3. Numerical Simulations

We carry out 2D kinetic simulations using the VPIC code (Bowers et al. 2008), which is a particle-in-cell code solving Maxwell's equations and the Vlasov equation in a fully relativistic manner. The simulations start from a force-free current sheet with $\mathbf{B} = B_0 \tanh(z/\lambda) \hat{x} + B_0 \sqrt{\text{sech}^2(z/\lambda) + B_g^2/B_0^2} \hat{y}$, where B_0 is the strength of the reconnecting magnetic field, B_g is the strength of the guide field and λ is the half-thickness of the current sheet. We choose $\lambda = d_i$ in all simulations, where $d_i = c/\omega_{pi} = c/\sqrt{4\pi n_i e^2/m_i}$ is the ion inertial length. A reduced proton to electron mass ratio $m_i/m_e = 25$ is used for all cases. The initial particle distributions are Maxwellian with uniform density n_0 and temperature $T_i = T_e = T_0$. Electrons drift with a velocity U_e that satisfies the Ampere's law. We vary plasma $\beta = 8\pi nk(T_e + T_i)/B_0^2$ by varying B_0 only, which will also change the Alfvén speed $v_A = B_0/\sqrt{4\pi n_0 m_i}$. The electron beta $\beta_e = 8\pi nk T_e/B_0^2$ ranges from 0.02 to 0.32. The guide field strength B_g is changed from 0 to B_0 . The parameters are listed in Table 1, which gives c/v_A , c/v_{the} , ω_{pe}/Ω_{ce} , β_e , and B_g/B_0 . We separate the runs into two groups: B1–3 indicate three runs with different plasma $\beta_e = 0.02$ –0.32; G1–4 indicate four runs with $B_g = 0 - B_0$. The domain sizes are $L_x \times L_z = 200d_i \times 100d_i$ for all simulations. The grid sizes are 4096×2048 for runs with $\beta_e = 0.02$, 2048×1024 for $\beta_e = 0.08$, and 1024×512 for $\beta_e = 0.32$. We use 200 particles per cell per species in the runs with $\beta_e = 0.02$, 400 for $\beta_e = 0.08$, and 800 for $\beta_e = 0.32$. For electric and magnetic fields, we employ periodic boundaries along the x -direction and perfectly conducting boundaries along the z -direction. For particles, we employ periodic boundaries along the x -direction and reflecting boundaries along the z -direction. Initially, a long wavelength perturbation with $B_z = 0.03B_0$ is added to induce reconnection (Birn et al. 2001).

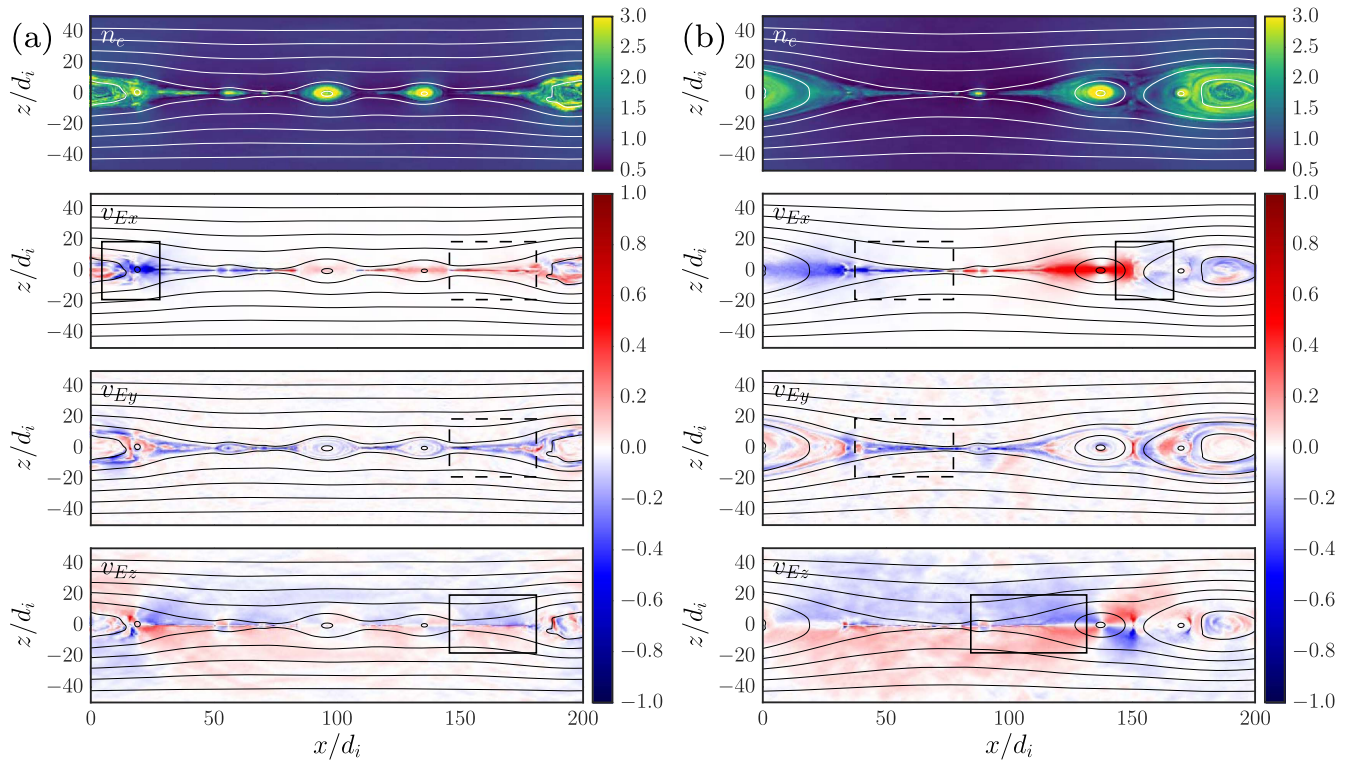


Figure 1. Electron density and three components of the v_E in run B1 ($\beta_e = 0.02$, $B_g = 0$) at $t\Omega_{ci} = 150$ (left) and 300 (right). n_e is normalized by the initial density n_0 . The velocity components are normalized by the upstream Alfvén speed. The boxes with solid outlines indicate representative regions with fluid compression, and boxes with dashed outlines indicate regions with velocity shear.

Table 1
List of Simulation Runs

Run	c/v_A	c/v_{the}	ω_{pe}/Ω_{ce}	β_e	B_g/B_0
B1/G1	5.0	7.07	1.0	0.02	0.0
B2	10.0	7.07	2.0	0.08	0.0
B3	20.0	7.07	4.0	0.32	0.0
G2	5.0	7.07	1.0	0.02	0.2
G3	5.0	7.07	1.0	0.02	0.5
G4	5.0	7.07	1.0	0.02	1.0

Note. $v_A = B_0/\sqrt{4\pi n_0 m_i}$ is the Alfvén speed of the inflow region. $v_{the} = \sqrt{2kT_e/m_e}$ is the electron thermal speed. $\omega_{pe} = \sqrt{4\pi n_0 e^2/m_e}$ is the electron plasma frequency. $\Omega_{ce} = eB/(m_e c)$ is the electron gyrofrequency. $\beta_e = 8\pi n_0 kT_e/B_0^2$ is the electron plasma β based on the reconnection component of the magnetic field. B_g is the guide field component of the magnetic field. B1–3 indicate runs with different plasma β . G1–4 indicate runs with different guide fields.

4. Results

4.1. Compression and Shear Regions

First, we describe regions with strong compression and shear, and their evolutions in our reconnection simulations. Figure 1 shows the electron density n_e and three components of v_E (v_{Ex} , v_{Ey} , and v_{Ez}) at two time frames (a) $t\Omega_{ci} = 150$ and (b) $t\Omega_{ci} = 300$ for Run B1/G1. As reconnection evolves, the current sheet breaks into a series of magnetic islands. During this process, the electron density can increase to over three times the initial value in reconnection exhausts and magnetic islands. The enhanced density indicates that plasma is compressed in the reconnection layer. The illustrated v_E components in Figure 1 further demonstrate this. We find that

reconnection exhausts, contacting islands, and island coalescence regions are the most important regions with strong compression. For example, the v_{Ex} panels show that the reconnection outflow is compressed in the island-merging regions; the v_{Ez} panels show that the reconnection inflow forms a compressed region at the center of the reconnection exhaust (both are indicated by boxes with solid outlines), leading to an enhanced electron density. Besides being compressed, the bulk flow is also experiencing strong shear at the reconnection exhaust boundaries and centers due to the gradient of v_{Ex} and v_{Ey} along the z -direction (boxes with dashed outlines). As we will show below, these compressed and sheared flows can lead to significant particle energization.

4.2. Electron Energy Spectra and Bulk Energization Due to Compression and Shear

Next, we consider the details of electron energization. Electrons are accelerated to higher energies during the reconnection processes. Figure 2(a) shows the electron energy spectra at $t\Omega_{ci} = 600$ in all of our simulations. High-energy tails (kinetic energy $\varepsilon > 20$ times that of the initial thermal energy ε_{th}) develop in all runs, and they are more prominent in low- β runs than runs with higher β . The high-energy tail extends up to $70\varepsilon_{th}$ for the run with $\beta_e = 0.08$ and only $25\varepsilon_{th}$ for the run with $\beta_e = 0.32$, and both the particle number and particle kinetic energy in the tails in these two runs are much less than 1% of those quantities in all of the simulations (Figures 2(b) and (c)). In contrast, for runs with $\beta_e = 0.02$, the high-energy tails extend up to $400\varepsilon_{th}$, contain 1.6%–5.0% of electrons by number (Figure 2(b)), and account for 12%–29% of the energy in all of the electron distributions (Figure 2(c)) depending on the guide field strength. Figure 2(a) shows that

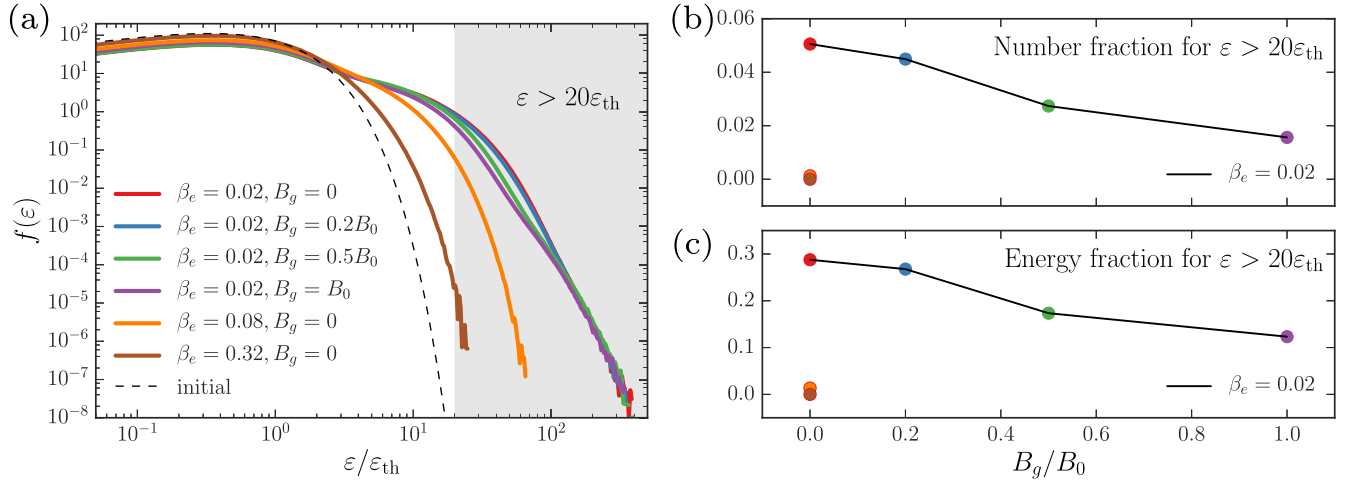


Figure 2. (a) Electron energy spectra for all runs at $t\Omega_{\text{ci}} = 600$. ε_{th} is the initial thermal energy. The dashed line shows the initial thermal distribution, which is the same for all runs. The shaded region indicates the electron distribution with $\varepsilon > 20\varepsilon_{\text{th}}$. (b) Number fraction of the electrons with $\varepsilon > 20\varepsilon_{\text{th}}$ among all electrons in the simulation box. The symbols are color-coded the same as those in (a). The solid line indicates the runs with $\beta_e = 0.02$. The orange and brown symbols at the bottom left corner indicate runs with $\beta_e = 0.08$ and 0.32 , respectively. (c) Energy fraction of the electrons with $\varepsilon > 20\varepsilon_{\text{th}}$.

the high-energy particle flux decreases with the guide field strength in $20\varepsilon_{\text{th}} < \varepsilon < 100\varepsilon_{\text{th}}$ and that the fluxes are almost the same for electrons with $\varepsilon > 100\varepsilon_{\text{th}}$. Our results show that electrons with $\varepsilon > 100\varepsilon_{\text{th}}$ only account for less than 0.004% of all electrons, so we focus on the energy range $20\varepsilon_{\text{th}} < \varepsilon < 100\varepsilon_{\text{th}}$, which is statistically more important in the following discussions.

To quantify the energization due to compression and shear effects, we calculate energization due to different fluid-motion terms such as compression, shear, and fluid inertia discussed in Section 2 (Equation (9)), as well as the contribution from agyrotropic particle distribution (Li et al. 2017). In Figure 3, we show the time evolution of each energization effect for runs G1 ($\beta_e = 0.02, B_g = 0$) and G3 ($\beta_e = 0.02, B_g = 0.5B_0$). The summation of different energization mechanisms (black line) agrees well with the energization due to the perpendicular electric field $\mathbf{j}_{\perp} \cdot \mathbf{E}_{\perp}$ (blue line with dots). The compressional energization (red line) is dominant when there is no guide field but becomes comparable to the shear energization (blue line) when $B_g = 0.5B_0$. The inertia term is negligible for electrons but becomes important for ions. (We will report the energization of ions elsewhere.) As the guide field gets stronger, both compression and shear terms are suppressed, and the energization due to parallel electric field dominates (Figure 4(a)). We found that the partition of these energization terms is similar in simulations with higher plasma β (Figure 4(b)), though the compression energization contributes less when β is high because plasma is less compressible (Birn et al. 2012). Another noticeable difference is that the energization in run B3, which has the highest $\beta_e = 0.32$, has a large contribution from the nongyrotropic effects, suggesting that electrons are not well magnetized when plasma β is high.

4.3. Spatial Distribution of Compression Energization and Shear Energization

Spatial distributions of different energization effects reveal that reconnection exhausts, contracting islands, and island-merging regions are the three most important regions for compression and shear acceleration. Figure 5 shows the energization terms in these regions in run G1 ($\beta_e = 0.02, B_g = 0$) at $t\Omega_{\text{ci}} = 150$. The bottom panel of Figure 5(a)

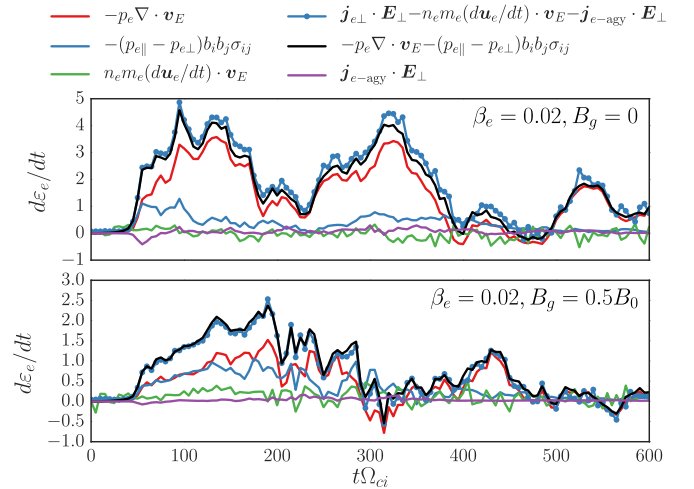


Figure 3. Time evolution of electron energization terms: compressional energization $-p_e \nabla \cdot \mathbf{v}_E$, shear energization $-(p_{e\parallel} - p_{e\perp}) b_i b_j \sigma_{ij}$, inertial energization $n_e m_e (d\mathbf{u}_e/dt) \cdot \mathbf{v}_E$, and agyrotropic energization $\mathbf{j}_{e-\text{agy}} \cdot \mathbf{v}_E$. The summation of $-p_e \nabla \cdot \mathbf{v}_E$ and $-(p_{e\parallel} - p_{e\perp}) b_i b_j \sigma_{ij}$ (black) is compared with the energization due to perpendicular electric field $\mathbf{j}_{\perp} \cdot \mathbf{E}_{\perp}$ subtracting the inertial and agyrotropic terms (blue with dots). Top panel: simulation without a guide field. Bottom panel: similar to the top panel, but for the simulation with a guide field $\sim 50\%$ of the reconnecting component.

shows that compressional energization (red) is the dominant term in these regions. In the contracting island ($x \sim 57d_i$), the compressional energization dominates as the energization primarily comes from the converging v_{Ex} and v_{Ez} . Detailed analysis shows that the converging v_{Ex} only contributes about 10% of the energization in the contracting island and that most of the energization is through converging v_{Ez} . We find that as the island moves leftward and interacts with the background plasma, v_{Ez} slightly diverges at the left-hand side of the island due to expansion along the z -direction, but the converging inflow v_{Ez} on the right-hand side contributes more, leading to a net energization. In the region of two merging islands (boxed region in Figure 5), compressional energization dominates and peaks at the right-hand side of the smaller island ($x \sim 20d_i$), where the reconnection outflow compresses the plasma in the island. Besides magnetic

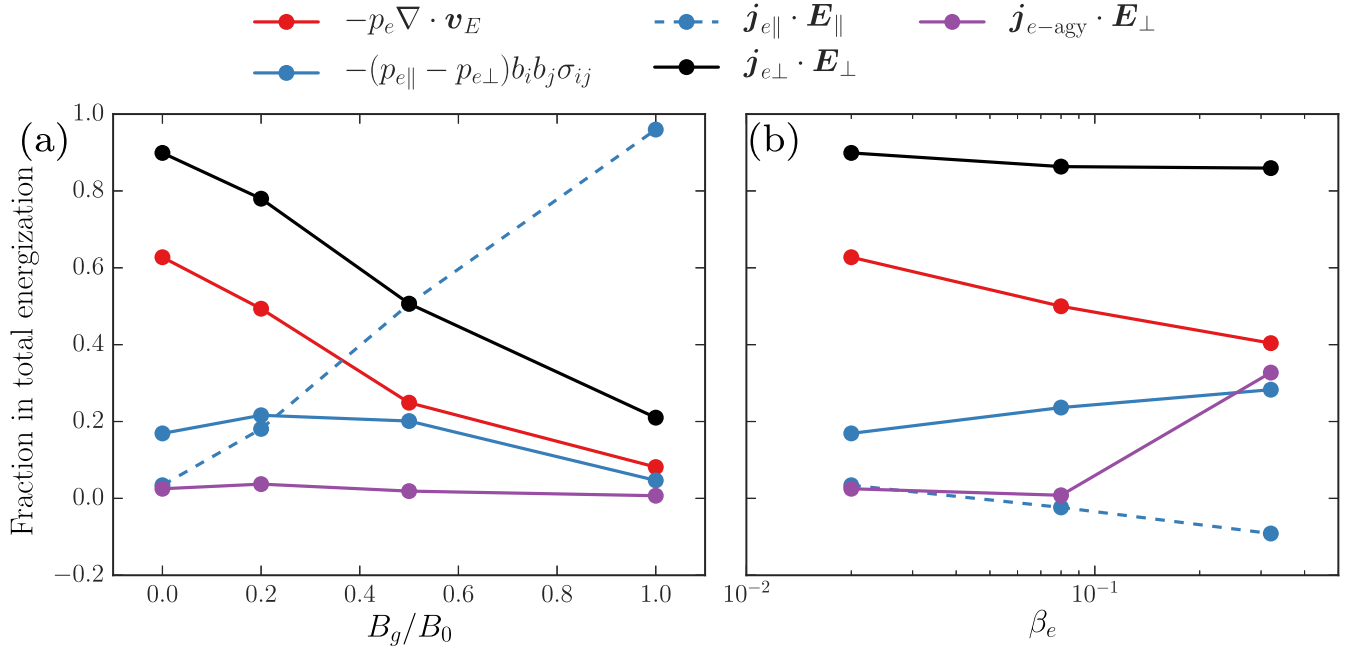


Figure 4. Energization terms for runs with different guide field B_g (a) and plasma β (b). The energization terms are integrated over the whole simulation box and time until $t_1 \Omega_{ci} = 600$ and then normalized by the total particle energy gain at t_1 . For example, $\mathbf{j}_{e\parallel} \cdot \mathbf{E}_\parallel$ represents $\int d^3r \int_0^{t_1} dt (\mathbf{j}_{e\parallel} \cdot \mathbf{E}_\parallel) / \Delta K_e(t_1)$. Note that the contributions tend to be underestimated due to the accumulated integration errors over time. See Table 1 for the parameters of those runs.

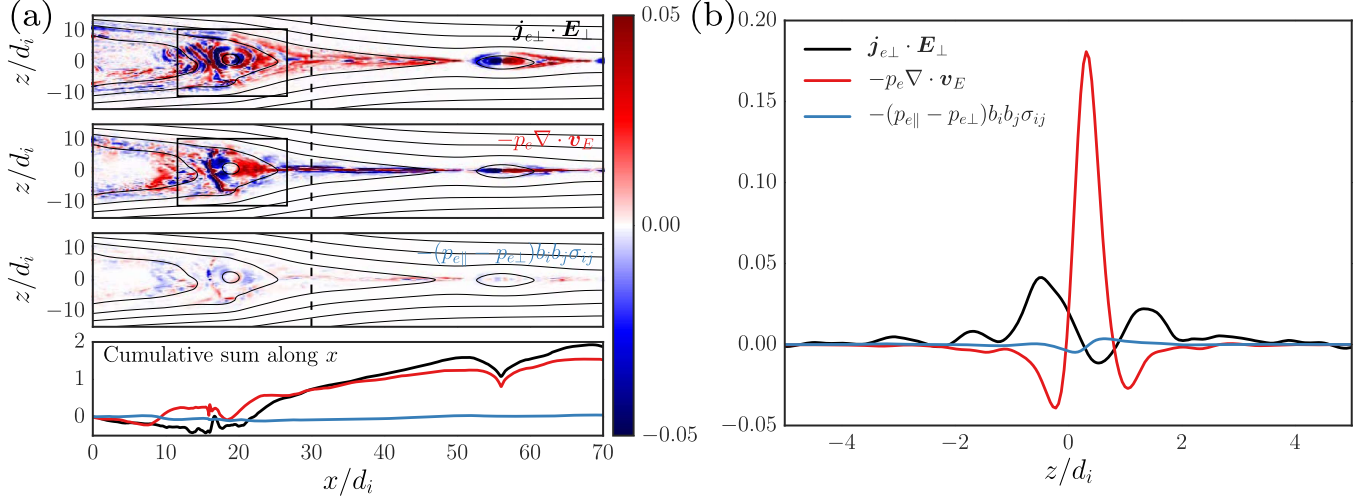


Figure 5. (a) Energization terms in run G1 ($\beta_e = 0.02$, $B_g = 0$) at $t^* \Omega_{ci} = 150$. The top three panels are energization due to perpendicular electric field, compression, and shear, respectively. The bottom panel shows the cumulative sum of these terms along the x -direction. The dashed lines indicate a cut along the z -direction. The energization terms are normalized by $en_0 v_A^2 B_0$, where n_0 is the initial electron number density, v_A is the Alfvén speed of the inflow plasma, and B_0 is the asymptotic magnetic field strength. In the boxed region, a smaller island on the right is merging with the large island. (b) The profile of the energization terms along the dashed lines in the left panels. The difference between perpendicular energization and the sum of compression and shear energizations is due to a flux term. See the text for a discussion.

islands, the reconnection exhaust is also efficient at energization, and the compressional energization dominates in these regions (e.g., $x \sim 30\text{--}50d_i$ in Figure 5). We find that $\mathbf{j}_{e\perp} \cdot \mathbf{E}_\perp$ spread throughout the whole region of a reconnection exhaust, while the energization due to compression is negative in most of the region, but is positive and peaks at the center $z = 0$ (Figure 5(b)), where v_{Ez} switches directions (Figure 1(a), bottom panel). The difference between these two terms is due to the flux term $\nabla \cdot (p_{e\perp} \mathbf{v}_E)$, which gives zero energization in a closed system as in our simulations.

Figure 5 also shows that compressional energization is nonuniform and is accompanied with expansion in some

regions. In the anti-reconnection layer ($x \sim 18d_i$), where these two islands merge, the overall compressional energization is small compared with other regions due to two reasons: the convergence of v_{Ex} is accompanied by the divergence of the outflow in the anti-reconnection region along the z -direction; the compression in the island on the right is accompanied by the expansion in the one on the left. More detailed trajectory analyses (e.g., Li et al. 2017) have found that some particles can get efficiently accelerated by accessing those compression regions.

Figure 5 suggests that shear energization is much weaker than compressional energization in those regions. More

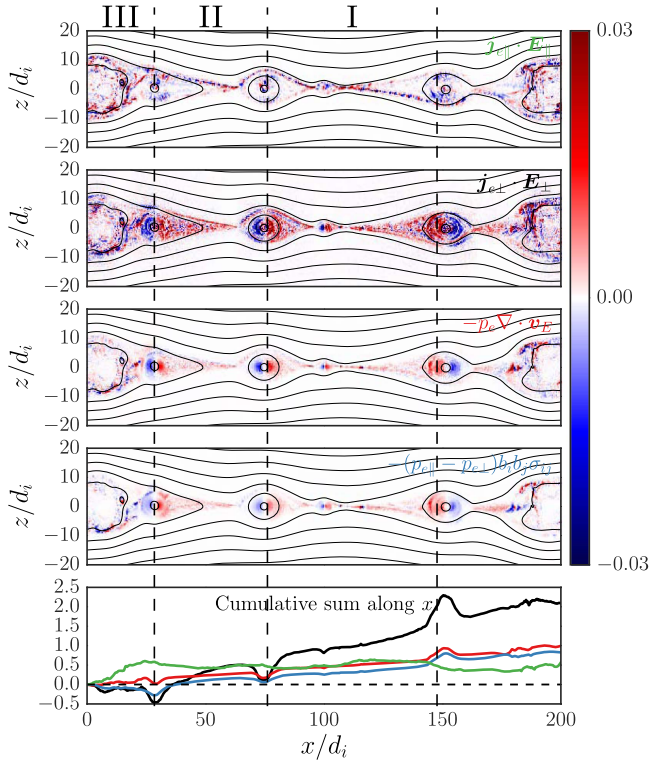


Figure 6. Energization terms in run G3 ($\beta_e = 0.02$, $B_g = 0.5B_0$) at $t\Omega_{ci} = 150$. The top four panels are energization terms by the parallel electric field, perpendicular electric field, compression, and shear. The bottom panel shows the cumulative sum of these terms along the x -direction. The vertical dashed lines separate three regions. Regions I and II are main reconnection sites, where the energization terms due to compression and shear dominate. Region III is a merging region of two magnetic islands, where the energization due to parallel electric field dominates. In region II, other terms are dominant. The energization terms are normalized by $en_0v_A^2B_0$, where n_0 is the initial electron number density, v_A is the Alfvén speed of the inflow plasma, and B_0 is the asymptotic magnetic field strength.

analyses have shown that the shear energization effect is weak in most regions either because the anisotropy is weak (e.g., in exhaust centers due to phase mixing; Egedal et al. 2015) or the shear term associated with magnetic field $b_i b_j \sigma_{ij}$ is small (e.g., along separatrix). Shear energization becomes comparable with the compressional energization when the guide field gets stronger (Figure 4(a)). Figure 6 shows the energization terms in run G3 ($\beta_e = 0.02$, $B_g = 0.5B_0$) at $t\Omega_{ci} = 150$. We find that the energization terms due to parallel electric field, compression, and shear are comparable but they peak in different regions. Those different effects accelerate particles in various locations. The parallel electric field accelerates particles along one side of the separatrix (Pritchett 2006). The compressional energization and shear energization are comparable in reconnection exhausts and magnetic islands but largely cancel each other in the anti-reconnection sites. The compressional energization is suppressed when compared with that in the run without a guide field (Figure 5), while the shear term increases due to stronger pressure anisotropy in simulations with a higher guide field (Le et al. 2013). The energization due to the parallel electric field is localized close to the main reconnection sites (e.g., region I in Figure 6) and the anti-reconnection sites (e.g., region III in Figure 6), where electrons are already energetic due to compressional energization and shear energization at earlier stages.

4.4. Energy Dependence of Compression Energization and Shear Energization

To characterize how these energization terms depend on particle energies, we calculate the contributions of individual particles according to different energization effects as described in Section 2 and accumulate them in a range of energy bins to obtain the distributions of these energization terms as a function of particle energy. Figures 7(a) and (b) show different energization effects and anisotropy as a function of energy at $t\Omega_{ci} = 150$ in run B1/G1 ($\beta_e = 0.02$, $B_g = 0$). Compressional energization dominates particle acceleration except for particles at low energies (\sim initial thermal energy ε_{th}). Those low-energy particles are energized close to X-points by the parallel electric field E_{\parallel} . Surprisingly, for particles with intermediate energies ($\sim 10\varepsilon_{th}$), the parallel electric field gives a cooling effect, and shear energization gives non-negligible acceleration. For high-energy particles ($>20\varepsilon_{th}$), compressional energization dominates, while the other two terms are negligible. Shear energization is ineffective for high-energy electrons because it requires anisotropy (Equation (9)) but the anisotropy for these high-energy electrons is less than 1.2 as shown in Figure 7(b).

The relative importance of the different energization mechanisms changes with the guide field strength. Figure 8 shows the distributions of these energization terms at $t\Omega_{ci} = 150$ (a) and 250 (b) for run G3 ($\beta_e = 0.02$, $B_g = 0.5B_0$). At $t\Omega_{ci} = 150$ (Figure 8(a)), compressional energization and shear energization are comparable for particles at different energies. This is because compressional energization is suppressed due to weak compressibility and shear energization is enhanced due to the large anisotropy (solid line in Figure 8(c)) when there is a finite guide field. At the same time, the parallel electric field accelerates low-energy electrons, decelerates intermediate-energy electrons, and accelerates high-energy electrons, but the energization is weaker than the other two terms. At $t\Omega_{ci} = 250$, the parallel electric field dominates the energization (Figure 8(b)) because it accelerates more high-energy electrons at the island-merging regions. The relative importance of each energization mechanism can be time variable (see below), as the newly formed current sheet breaks into islands and major island coalescence occurs when the islands interact with the large island as a consequence of our periodic simulation domain. However, even though the parallel electric field dominates the acceleration of high-energy particles at later stages in our setup, shear energization is still larger than the energization due to E_{\parallel} for particles at very high energies ($>50\varepsilon_{th}$). Shear energization is important for these electrons because they have a fairly large anisotropy (>1.5 , thick dashed line in Figure 8(c)) compared with that in the run without a guide field (Figure 7(b)). These results show that compressional energization and shear energization are still important for producing energetic electrons in reconnection with a moderate guide field ($B_g = 0.5B_0$), while the parallel electric field becomes more important.

4.5. Time Evolution of Compression Energization and Shear Energization

Figure 9 shows the time evolution of different energization terms for high-energy electrons ($>20\varepsilon_{th}$) in three runs with different guide fields (a) $B_g = 0$, (b) $B_g = 0.2B_0$, and (c)

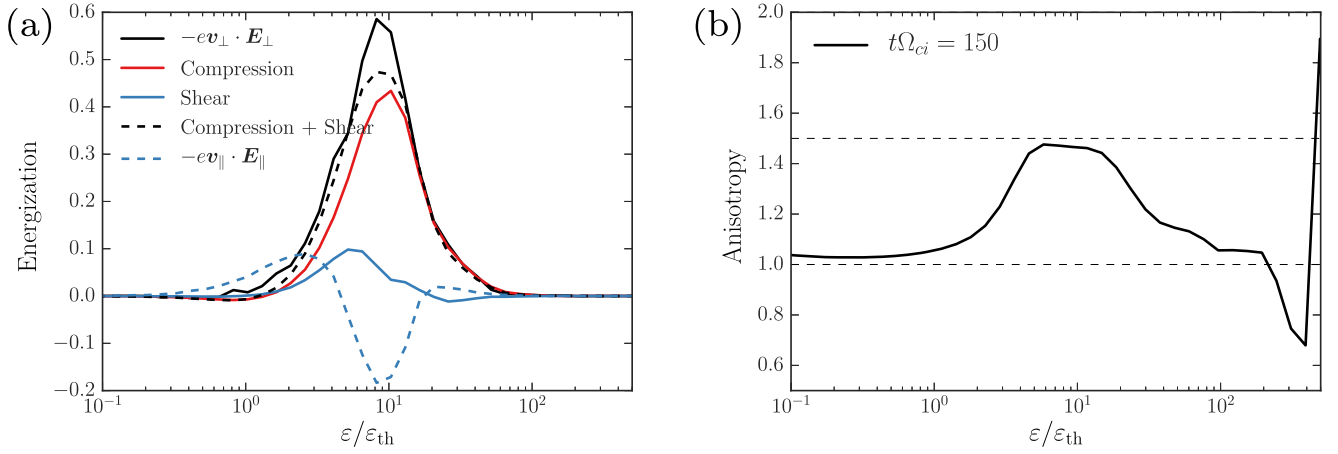


Figure 7. (a) Energy dependence of particle energization due to parallel electric field, perpendicular electric field, compression, and shear at $t\Omega_{ci} = 150$ for run B1/G1 ($\beta_e = 0.02$, $B_g = 0$). The black dashed line indicates the sum of the energization due to compression and shear. ε_{th} indicates the initial thermal energy. (b) Anisotropy for electrons with different energies. The anisotropy is defined as $\sum(|v_{\parallel} - v_{s\parallel}| \cdot (p_{\parallel} - p_{s\parallel}) / \sum(0.5(v_{\perp} - v_{s\perp}) \cdot (p_{\perp} - p_{s\perp}))$, where we sum over all electrons in an energy bin. The two dashed lines indicate anisotropy levels 1.0 and 1.5, in which 1.0 indicates the distribution is isotropic. Note that the peak at the highest energy bin is due to statistical error generated by merely a few electrons.

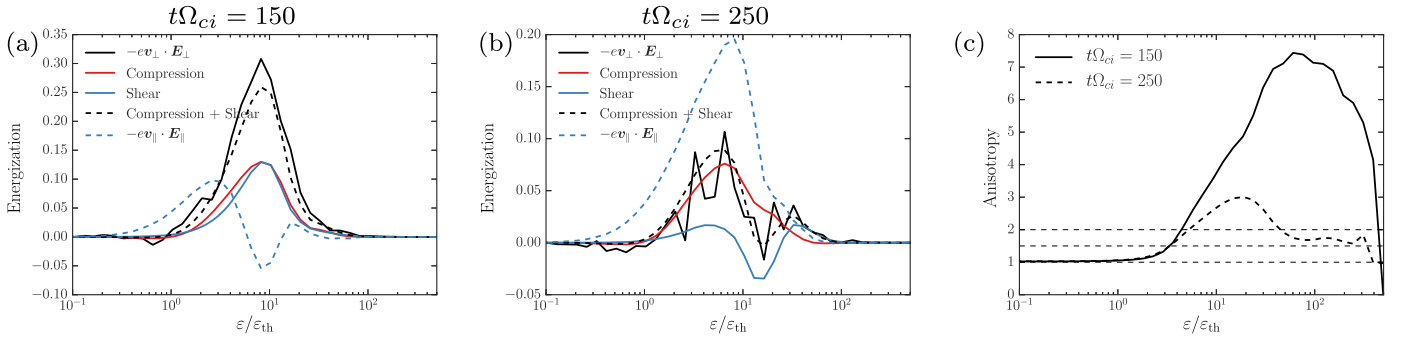


Figure 8. Energy dependence of particle energization due to parallel electric field, perpendicular electric field, compression, and shear at (a) $t\Omega_{ci} = 150$ and (b) $t\Omega_{ci} = 250$ for run G3 ($\beta_e = 0.02$, $B_g = 0.5B_0$). The black dashed line indicates the sum of the energization due to compression and shear. ε_{th} indicates the initial thermal energy. (c) Anisotropy for electrons with different energies. The anisotropy is defined as $\sum(|v_{\parallel} - v_{s\parallel}| \cdot (p_{\parallel} - p_{s\parallel}) / \sum(0.5(v_{\perp} - v_{s\perp}) \cdot (p_{\perp} - p_{s\perp}))$, where we sum over all electrons in an energy bin. The solid line is for $t\Omega_{ci} = 150$ frame. The thick dashed line is for $t\Omega_{ci} = 250$ frame. The three thin dashed lines indicate anisotropy levels 1.0, 1.5, and 2.0, in which 1.0 indicates that the distribution is isotropic.

$B_g = 0.5B_0$. In simulations without a guide field (Figure 9(a)) or with a weak guide field (Figure 9(b)), compressional energization dominates throughout the simulation. In simulations with a moderate guide field (Figure 9(c)), compressional energization and shear energization are comparable. The sum of these two terms contribute over 80% of the energization at the beginning of the simulation ($t\Omega_{ci} < 200$), when the main reconnection layer (excluding the largest island at the left and right boundaries) is the major energization site (Figure 6). The energization due to parallel electric field contributes over 70% of the total energization at $200 < t\Omega_{ci} < 350$, when smaller islands (at $x = 75d_i$ and $150d_i$ in Figure 6) merge with the largest island. As discussed in the previous paragraph, the time variation is likely dependent on the detailed plasma dynamics such as the development of new sheet, island formation, and island coalescence in a cyclic way. In a more realistic setup with open boundaries (Daughton et al. 2006), magnetic islands grow and are then ejected out of the system. In that situation, we expect a more evenly distributed energization over time.

5. Discussion and Conclusion

In this work, we have studied the particle energization in magnetic reconnection and demonstrated that the energization

associated with particle drift motions can be described as energization processes due to fluid compression and shear, especially when the system size is large enough. The shear energization is associated with an anisotropic particle velocity distribution. By means of fully kinetic simulations, we find that the compressional energization dominates the energization processes in reconnection in a low- β plasma with a weak guide field (≤ 0.2 times the reconnecting component) and becomes comparable with shear energization in reconnection with a moderate guide field (50% of the reconnecting component); the sum of these two terms dominates the acceleration of high-energy particles (> 20 times of the initial thermal energy) except in the case with a strong guide field, in which the acceleration due to the parallel electric field dominates.

Our analyses have shown that the compressional energization is associated with fluid compression along both the reconnection inflow and outflow directions. We find that the compressional energization is suppressed in simulations with an increasing guide field and the shear energization is not suppressed until the guide field is comparable to the reconnecting magnetic field ($B_g = B_0$). The 2D plots (Figures 5 and 6) show that the compressional energization and shear energization are not cospatial with the previously

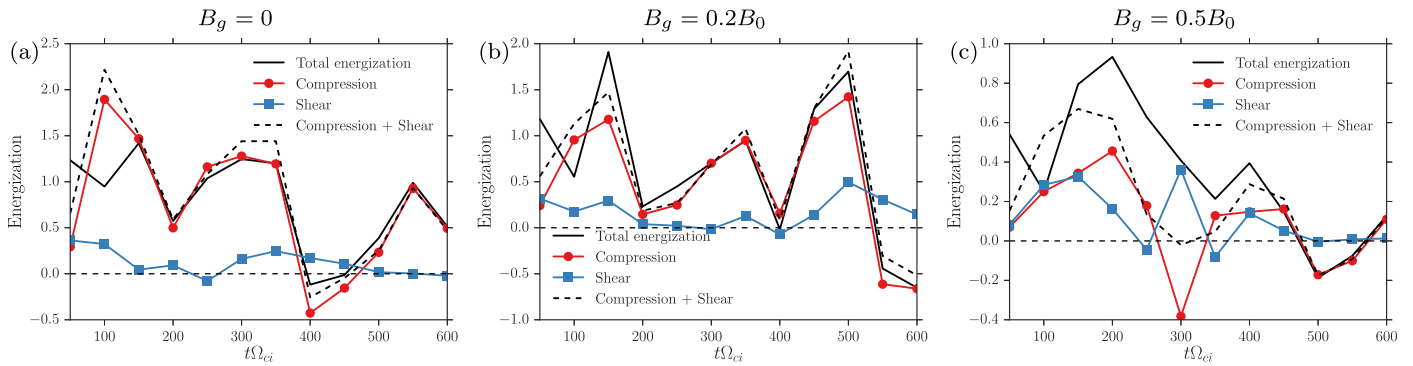


Figure 9. Time evolution of compressional energization and shear energization for high-energy electrons (>20 times of the initial thermal energy) in (a) run B1/G1, (b) run G2, and (c) run G3. The black dashed line is the sum of these two terms. The black solid line is the total energization by summing $e\mathbf{v} \cdot \mathbf{E}$ over all high-energy electrons. Run G4 ($B_g = B_0$) is not shown here because the parallel energization dominates throughout the simulation. Run B2 ($\beta_e = 0.08$) is not shown because its energization process is similar to run B1/G1. Run B3 ($\beta_e = 0.32$) is not shown because very few particles can be accelerated to over 20 times the initial thermal energy.

studied energization term $\mathbf{j} \cdot \mathbf{E}$ because a flux term $\nabla \cdot (p_{s\perp} \mathbf{v}_E)$ was not considered (Li et al. 2015, 2017). We find that the inertial energization term is small compared with other terms for electrons because of small electron mass but can contribute over 20% of energization for ions (Li et al. 2017). We will discuss its effect on high-energy ion acceleration in a future study.

The connection between particle drifts and compression is consistent with previous results in energetic particle transport theory (Jokipii 1982; Jones 1990; le Roux et al. 2015). Our results on energization processes are consistent with Birn et al. (2012), who performed MHD simulations and demonstrated that fluid compression is the leading mechanism for plasma energization in low- β plasma with a low guide field. These results differ from some previous modeling works, in which the authors assumed that the reconnection layer is incompressible (Bian & Kontar 2013; Drake et al. 2013). Compressibility has been emphasized in recent models of particle energization in magnetic reconnection (le Roux et al. 2015; Montag et al. 2017). This work provides the first quantitative evaluation of the role of compressibility in fully kinetic simulations. Also, the plasma energization described by Equation (9) is consistent with the general analytical theory by Montag et al. (2017) (see the Appendix) based on double-adiabatic assumptions.

The anisotropic momentum distribution of energetic particles is important for shear acceleration. Our 2D kinetic simulations show that this leads to non-negligible acceleration when a moderate guide field exists. The anisotropic distribution can be generated by electron trapping (Egedal et al. 2013) and curvature/gradient drift motions (Drake et al. 2010; le Roux et al. 2015). The anisotropy tends to be weakened when the particle orbits are chaotic in the weak guide field limit or if the strong wave-particle interaction presents. Quantifying the role of anisotropic distribution in energetic particle acceleration in the reconnection region is an important problem for future studies.

Our 2D kinetic simulations have a few limitations. First, we are forced to use a relatively low-mass ratio $m_i/m_e = 25$ in order to capture the long-term energy conversion in low- β reconnection with a fairly large simulation domain, but the plasma dynamics and field structures might change with the mass ratio, especially for simulations with a guide field (Le et al. 2013). The second limitation is that the 2D configuration prevents the gradient of fluid velocity along the out-of-plane direction, and this might

influence the energization due to fluid compression and shear. Also, a real 3D configuration leads to the development of turbulence (Bowers & Li 2007; Daughton et al. 2011; Liu et al. 2011; Guo et al. 2015), which can scatter particles and reduce pressure anisotropy. Another limitation is that the drift analysis does not include compression of fluid velocity along the magnetic field direction. This is usually achieved through wave-particle interaction and is out of the scope of the current study. We defer these studies to a future work.

To conclude, we find that the compressional energization and shear energization are the major mechanisms for high-energy particle acceleration during reconnection in a plasma with low- β and a weak or moderate guide field and the shear energization is proportional to the pressure anisotropy. This study links the acceleration mechanisms found in kinetic simulations with that in energetic particle transport theory (e.g., Parker 1965; Drake et al. 2013; Zank 2014; le Roux et al. 2015). It provides clues for building an energetic particle transport model for particle acceleration in solar flares and other astrophysical reconnection sites.

We acknowledge the support by NASA under grant NNH16AC60I, DOE OFES, and the support by the DOE through the LDRD program at LANL. F.G.'s contributions are partly based upon work supported by the U.S. Department of Energy, Office of Fusion Energy Science, under Award Number DE-SC0018240. We gratefully acknowledge our discussions with Xiangrong Fu and Andrey Beresnyak. Simulations were performed with LANL institutional computing and at the National Energy Research Scientific Computing Center.

Appendix Comparison of Energization between Double-adiabatic Theories and the Current Analysis

By assuming that particles are magnetized and neglecting the heat flux (Chew et al. 1956), Montag et al. (2017) showed that the energization for a single energetic particle is [their Equation (12)]

$$\frac{dU}{dt} = -m v_{\parallel}^2 \left[\frac{\dot{B}}{B} \left(1 - \frac{v_{\perp}^2}{2v_{\parallel}^2} \right) - \frac{\dot{n}}{n} \right], \quad (10)$$

where U is the total particle energy, m is the particle mass, B is the magnetic field strength, $\dot{B} \equiv dB/dt$, n is the plasma

density, $\dot{n} \equiv dn/dt$, and v_{\parallel} and v_{\perp} are the parallel and perpendicular particle velocities, respectively. From the continuity equation, we get $\dot{n}/n = -\nabla \cdot \mathbf{V}$, where \mathbf{V} is plasma velocity. From the induction equation $\partial \mathbf{B}/\partial t = \nabla \times (\mathbf{V} \times \mathbf{B})$ (Chew et al. 1956),

$$\frac{\dot{\mathbf{B}}}{B} = -\nabla \cdot \mathbf{V} + b_i b_j \frac{\partial V_i}{\partial x_j}. \quad (11)$$

Integrating Equation (10) over the velocity space, we get the total particle energization

$$\frac{d\mathcal{E}}{dt} = -(p_{\parallel} - p_{\perp}) \left(-\nabla \cdot \mathbf{V} + b_i b_j \frac{\partial V_i}{\partial x_j} \right) - p_{\parallel} \nabla \cdot \mathbf{V}, \quad (12)$$

where \mathcal{E} is the particle energy density, p_{\parallel} and p_{\perp} are the parallel and perpendicular pressures, respectively, and

$$\begin{aligned} \frac{\partial V_i}{\partial x_j} &= \frac{1}{3} \frac{\partial V_k}{\partial x_k} \delta_{ij} + \frac{1}{2} \left(\frac{\partial V_i}{\partial x_j} + \frac{\partial V_j}{\partial x_i} - \frac{2}{3} \frac{\partial V_k}{\partial x_k} \delta_{ij} \right) \\ &+ \frac{1}{2} \left(\frac{\partial V_i}{\partial x_j} - \frac{\partial V_j}{\partial x_i} \right) \end{aligned} \quad (13)$$

$$= \frac{1}{3} \nabla \cdot \mathbf{V} \delta_{ij} + \sigma_{ij} + \omega_{ij}, \quad (14)$$

where σ_{ij} is the shear tensor and ω_{ij} is the rotation tensor. Then,

$$\frac{d\mathcal{E}}{dt} = -\frac{p_{\parallel} + 2p_{\perp}}{3} \nabla \cdot \mathbf{V} - (p_{\parallel} - p_{\perp}) b_i b_j \sigma_{ij}, \quad (15)$$

$$= -p \nabla \cdot \mathbf{V} - (p_{\parallel} - p_{\perp}) b_i b_j \sigma_{ij}, \quad (16)$$

where we used $b_i b_j \omega_{ij} = 0$. This is consistent with the dominant energization terms in Equation (9).

ORCID iDs

Xiaocan Li  <https://orcid.org/0000-0001-5278-8029>

Fan Guo  <https://orcid.org/0000-0003-4315-3755>

Hui Li  <https://orcid.org/0000-0003-3556-6568>

Joachim Birn  <https://orcid.org/0000-0002-1496-4076>

References

- Beresnyak, A., & Li, H. 2016, *ApJ*, **819**, 90
 Bian, N. H., & Kontar, E. P. 2013, *PhRvL*, **110**, 151101
 Birn, J., Borovsky, J. E., & Hesse, M. 2012, *PhPI*, **19**, 082109
 Birn, J., Drake, J. F., Shay, M. A., et al. 2001, *JGR*, **106**, 3715
 Blandford, R., & Eichler, D. 1987, *PhR*, **154**, 1
 Bowers, K., & Li, H. 2007, *PhRvL*, **98**, 035002
 Bowers, K. J., Albricht, B. J., Yin, L., Bergen, B., & Kwan, T. J. T. 2008, *PhPI*, **15**, 055703
 Caspi, A., & Lin, R. P. 2010, *ApJL*, **725**, L161
 Chew, G. F., Goldberger, M. L., & Low, F. E. 1956, *RSPSA*, **236**, 112
 Dahlin, J. T., Drake, J. F., & Swisdak, M. 2014, *PhPI*, **21**, 092304
 Daughton, W., Roytershteyn, V., Karimabadi, H., et al. 2011, *NatPh*, **7**, 539
 Daughton, W., Scudder, J., & Karimabadi, H. 2006, *PhPI*, **13**, 072101
 de Gouveia Dal Pino, E. M., & Kowal, G. 2015, *ASSL*, **407**, 373
 Drake, J. F., Opher, M., Swisdak, M., & Chamoun, J. N. 2010, *ApJ*, **709**, 963
 Drake, J. F., Shay, M. A., Thongthai, W., & Swisdak, M. 2005, *PhRvL*, **94**, 095001
 Drake, J. F., Swisdak, M., Che, H., & Shay, M. A. 2006, *Natur*, **443**, 553
 Drake, J. F., Swisdak, M., & Fermo, R. 2013, *ApJL*, **763**, L5
 Drury, L. O. 2012, *MNRAS*, **422**, 2474
 Earl, J. A., Jokipii, J. R., & Morfill, G. 1988, *ApJL*, **331**, L91
 Egedal, J., Daughton, W., & Le, A. 2012, *NatPh*, **8**, 321
 Egedal, J., Daughton, W., Le, A., & Borg, A. L. 2015, *PhPI*, **22**, 101208
 Egedal, J., Le, A., & Daughton, W. 2013, *PhPI*, **20**, 061201
 Fu, X. R., Lu, Q. M., & Wang, S. 2006, *PhPI*, **13**, 012309
 Guo, F., Li, H., Daughton, W., & Liu, Y.-H. 2014, *PhRvL*, **113**, 155005
 Guo, F., Liu, Y.-H., Daughton, W., & Li, H. 2015, *ApJ*, **806**, 167
 Hazeltine, R. D., & Meiss, J. D. 2003, *Plasma Confinement* (New York: Dover)
 Hoshino, M., Mukai, T., Terasawa, T., & Shinohara, I. 2001, *JGR*, **106**, 25979
 Jokipii, J. R. 1982, *ApJ*, **255**, 716
 Jones, F. C. 1990, *ApJ*, **361**, 162
 Krucker, S., & Battaglia, M. 2014, *ApJ*, **780**, 107
 Krucker, S., Hudson, H. S., Glesener, L., et al. 2010, *ApJ*, **714**, 1108
 Kulsrud, R. 1983, in *Handbook of Plasma Physics*, ed. M. N. Rosenbluth & R. Z. Sagdeev (New York: North-Holland), 115
 Le, A., Egedal, J., Ohia, O., et al. 2013, *PhRvL*, **110**, 135004
 le Roux, J. A., & Webb, G. M. 2009, *ApJ*, **693**, 534
 le Roux, J. A., Zank, G. P., Webb, G. M., & Khabarova, O. 2015, *ApJ*, **801**, 112
 Li, X., Guo, F., Li, H., & Li, G. 2015, *ApJL*, **811**, L24
 Li, X., Guo, F., Li, H., & Li, G. 2017, *ApJ*, **843**, 21
 Lin, R. P., & Hudson, H. S. 1976, *SoPh*, **50**, 153
 Liu, W., Li, H., Yin, L., et al. 2011, *PhPI*, **18**, 052105
 Longcope, D. W., Des Jardins, A. C., Carranza-Fulmer, T., & Qiu, J. 2010, *SoPh*, **267**, 107
 Montag, P., Egedal, J., Lichko, E., & Wetheron, B. 2017, *PhPI*, **24**, 062906
 Nalewajko, K., Uzdensky, D. A., Cerutti, B., Werner, G. R., & Begelman, M. C. 2015, *ApJ*, **815**, 101
 Oka, M., Ishikawa, S., Saint-Hilaire, P., Krucker, S., & Lin, R. P. 2013, *ApJ*, **764**, 6
 Oka, M., Krucker, S., Hudson, H. S., & Saint-Hilaire, P. 2015, *ApJ*, **799**, 129
 Oka, M., Phan, T.-D., Krucker, S., Fujimoto, M., & Shinohara, I. 2010, *ApJ*, **714**, 915
 Parker, E. N. 1965, *P&SS*, **13**, 9
 Pritchett, P. L. 2006, *JGRA*, **111**, 10212
 Provornikova, E., Laming, J. M., & Lukin, V. S. 2016, *ApJ*, **825**, 55
 Skilling, J. 1975, *MNRAS*, **173**, 245
 Wang, H., Lu, Q., Huang, C., & Wang, S. 2016, *ApJ*, **821**, 84
 Webb, G. M., Le Roux, J. A., & Zank, G. P. 2009, in *AIP Conf. Ser.* 1183, 18th Annual International Astrophysics Conf., ed. X. Ao & G. Z. R. Burrows (Melville, NY: AIP), 85
 Zank, G. P., Hunana, P., Mostafavi, P., et al. 2015, *ApJ*, **814**, 137
 Zank, G. P., le Roux, J. A., Webb, G. M., Dosch, A., & Khabarova, O. 2014, *ApJ*, **797**, 28
 Zank, G. P. (ed.) 2014, *LNP*, **877**
 Zhou, X., Büchner, J., Bárta, M., Gan, W., & Liu, S. 2015, *ApJ*, **815**, 6
 Zweibel, E. G., & Yamada, M. 2009, *ARA&A*, **47**, 291